

# Geochemical and geophysical effects of tectonic activity in faulted areas of the North China Craton

Zhi Chen<sup>a,\*</sup>, Ying Li<sup>a,\*</sup>, Zhaofei Liu<sup>a</sup>, Hongyi He<sup>a</sup>, Giovanni Martinelli<sup>b</sup>, Chang Lu<sup>a</sup>, Zihan Gao<sup>a</sup>

<sup>a</sup> CEA key Laboratory of Earthquake Prediction, Institute of Earthquake Forecasting, Beijing 100036, China

<sup>b</sup> INGV-National Institute of Geophysics and Volcanology Dept. of Palermo, Palermo 90146, Italy

## ARTICLE INFO

Editor: Dr Don Porcelli

### Keywords:

Fluid geochemistry  
Tectonic activity  
North China Craton  
Northeastern Tibetan Plateau  
Zhang-Bo seismic zone

## ABSTRACT

Fluid geochemistry in active fault zones has been proven to be sensitive to tectonic activity. The North China Craton (NCC) has attracted much attention because of its complex and intense tectonic activity. In this study, fluid geochemistry in the primary active fault zones in the NCC was investigated, including inference of its tectonic activity. Stronger degassing from soil and springs has been observed in the northeastern Tibetan Plateau (NETP) and the Zhang-Bo seismic zone (ZBSZ) than in the other seismic zones. Both geological soil gas and deep-derived gas (crust- or mantle-derived gas) from springs were concentrated there. Also, a comprehensive analysis has indicated that the development of new fractures might have occurred widely beneath the NETP and ZBSZ because of the strong regional tectonic activity there. The  $^3\text{He}/^4\text{He}$  and  $^4\text{He}/^{20}\text{Ne}$  of gas from the springs in the ZBSZ suggest that the low-velocity zone 20–40 km deep might be a magmatic intrusion derived from the mantle. However, crust-derived gas accompanied with a negligible mantle-derived component has been detected in the Diebu-Bailongjiang fault (DBF), the West Qinling fault (WQLF), and the Liupanshan fault (LPSF) in the NETP. There, the occurrence of more new fractures was probable, in accordance with the obvious  $\delta^{18}\text{O}$  shift of the water from the springs in the fault zones. This suggests that a channel flow, also depicted by the low-velocity zone 20–40 km deep, could have formed within the crust and that the probable leading front reached the LPSF.

## 1. Introduction

The NCC was formed about 1.85 Ga ago and has attracted much attention because of its dramatic tectonic activity and complex geochemical characteristics of fluid trapped in the basement rocks and degassing within the fault zones (Chen and Ai, 2009; Chen et al., 2018). The NCC was destroyed in the Late Mesozoic subject to the combined action of collision between the North China and Yangtze blocks and subduction westward of the paleo-Pacific plate (Zhu et al., 2012), according to numerous previous studies focusing on regional magmatism, tectonic deformation and lithospheric structure (Zheng et al., 2009; Zhai and Santosh, 2013), and became active and presented regional rotation within the plate since the Early Cretaceous (Wu et al., 2005), which contradicted the classical plate tectonic theory stating that the stability was an inherent property of Craton (Perchuk et al., 2020). Additionally, significant differences in lithospheric structure and tectonic activity between the eastern and western segments of the NCC emerged after the destruction of the NCC (Chen et al., 2014). Attributed to the weak extensional deformation in the Early Cretaceous (Zhai and Liu, 2003;

Zhai, 2019), the western segment of the NCC presented a framework of huge basins, where depression or fracture-depression occurred, and volcanism and tectonic activity were not active there, indicating its stability properties (Zhu et al., 2012), while the eastern segment was active, where ductile tectonic deformation, crustal remelting, weakening, thinning and extension, and low velocity within the lithosphere were occurred extensively (Zheng et al., 2015). Its tectonic state was variable (Zhao et al., 2017), volcanism with high-K calc-alkaline magma was drastic there in the Early Cretaceous, while it quietened down in the Cenozoic (Chen et al., 2005). Therefore, further implementation of active state investigation for the NCC is needed, which could be of great significance and essential for understanding and establishing a new continental evolution theory.

Earth is an open system, and fluid release is a major means of exchanging matter and energy at various depths (Tao, 2005). An active fault system and its associated fracturing play a fundamental role in deep fluids such as  $\text{CO}_2$ , Rn, and He ascending toward the surface by creating pathways that extend from the deep lithosphere to the earth's surface. Deep fluids can migrate upward through those pathways

\* Corresponding authors.

E-mail addresses: [dugu\\_830822@163.com](mailto:dugu_830822@163.com) (Z. Chen), [subduction6@hotmail.com](mailto:subduction6@hotmail.com) (Y. Li).

<https://doi.org/10.1016/j.chemgeo.2022.121048>

Received 15 February 2022; Received in revised form 16 July 2022; Accepted 2 August 2022

Available online 6 August 2022

0009-2541/© 2022 Elsevier B.V. All rights reserved.

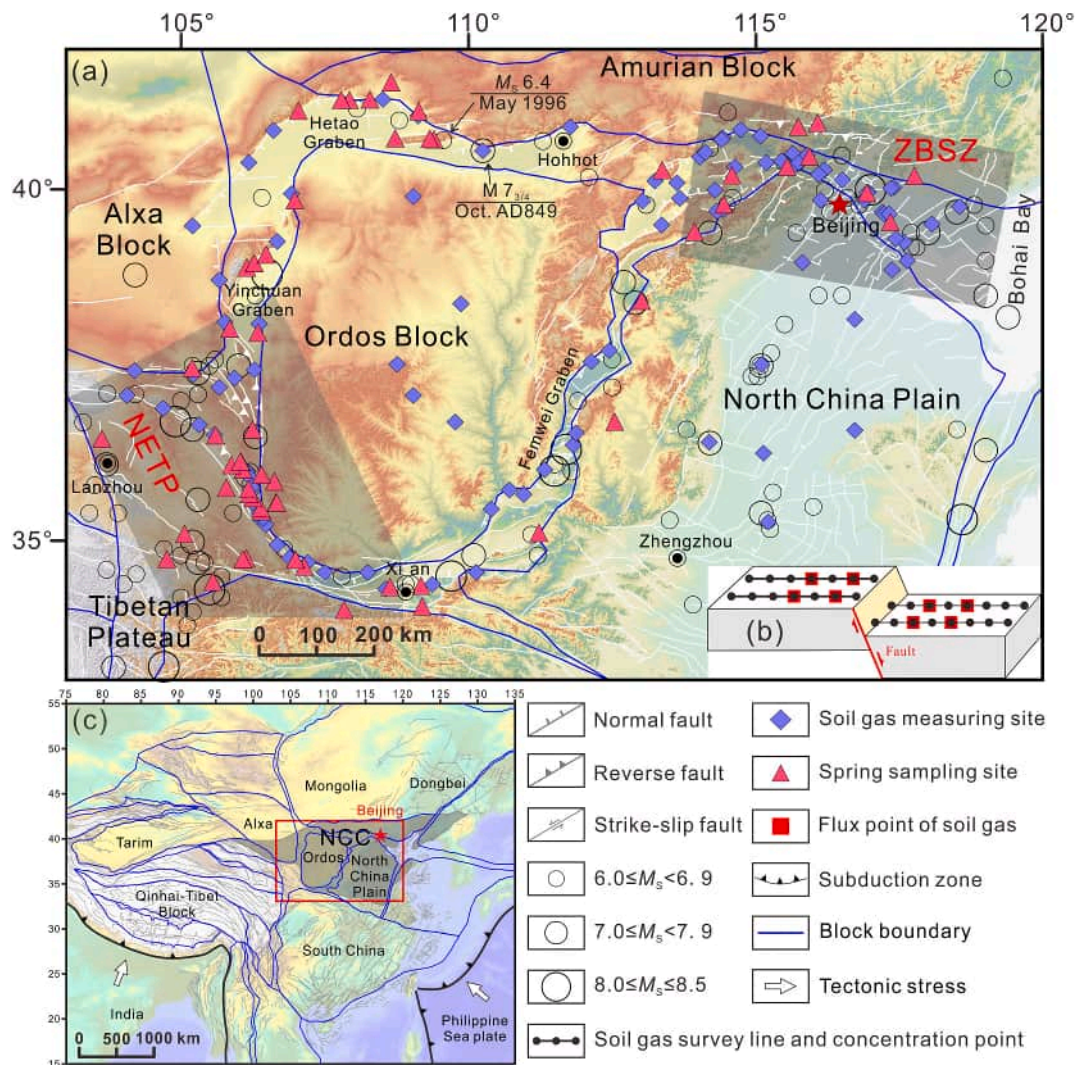


**Fig. 1.** Regional map of the study area. (a) shows the geological setting and measuring sites in the study area, (b) shows the layout of soil gas survey line, concentration and flux measuring points, (c) shows the location of the study region in China. Earthquakes were recorded from 780 BCE to 2020 (<http://news.ceic.ac.cn>).

because of their enhanced permeability and porosity relative to unfractured rock, and those fluids can carry specific geochemical information about the physicochemical evolution in the deep lithosphere (Yuce et al., 2014; D'Alessandro et al., 2020; Chen et al., 2019; Zhang et al., 2021).

Numerous field investigations have provided evidence that observing the geochemical characteristics of fluid emissions from the fault zone could be a potential proxy for investigation of physicochemical evolution in the lithosphere (Bedrosian et al., 2004; Faulkner et al., 2010; Yuce et al., 2017), which has made a significant contribution to the evaluation of mineral resources and modeling of geothermal water circulation (Pang et al., 2018), monitoring of geodynamic processes, revealing hidden faults, monitoring fault activity (Bonforte et al., 2013; Yuce et al., 2017; Yang et al., 2018), investigating strain accumulation and tectonic destruction (Bonforte et al., 2013; Chen et al., 2015), monitoring volcanic activity (Neri et al., 2016), monitoring seismic activity (Martinelli and Tamburello, 2020), and earth degassing investigation (Chen et al., 2018; Tamburello et al., 2018). Also, extensive laboratory experiments have been conducted concerning gas emission during rock failure and geochemical variations in the process of water-rock interactions under crustal conditions (Koike et al., 2015; Sun et al., 2016a). They have offered an experimental and physical basis for monitoring characteristic geochemical variation in the tectonic zone, which could provide information about the geodynamic processes in the

deep earth (Roeloffs, 1999; Girault et al., 2017).

Fluid geochemistry investigations had been widely implemented in the Cratons to study the destruction, regional tectonic activities, and mechanism of fluid genesis and transportation (Crossey et al., 2009; Shen et al., 2013; Zhang et al., 2016; Muirhead et al., 2020). Combined with isotope correlation diagrams, the noble gas isotopes in corundum and peridotite xenoliths provided unique and important constraints for comprehensive refertilization of lithospheric mantle in the eastern North China Craton (He et al., 2011). Xu et al. (2014) determined that the helium found in fluid collected from the crust in the Eastern Block (EB) was derived from the mantle and that active fault acted as an important pathway for mantle-derived ascending toward the surface in the nonvolcanic regions. The gas geochemistry investigation confirmed that deep fluid was active in the eastern NCC, and the degassing of mantle-derived gas could be a widespread occurrence in the EB and Trans-North China Orogen (TNCO) (Lu et al., 2021).

In this study, the distribution of geochemical characteristics of fluid within the principal active fault zones in the NCC was investigated, and the geochemical and geophysical effects of tectonic activity in faulted areas of the NCC were discussed.

## 2. Geological setting

Archean Cratons are stable tectonic units characterized by a cold,

**Table 1**

Statistical data on concentrations and fluxes of soil gas Rn and CO<sub>2</sub> from the active fault zones in the NCC.

Parameter	Zhang-Bo seismic zone	Ordos basin	Northeastern Tibetan Plateau	The other fault zones
Profile number	40	5	23	32
Concentration number	600	75	345	480
Flux number	160	20	92	128
C <sub>Rn</sub> Mean (kBq m <sup>-3</sup> )	3.80–37.89	3.22–8.35	4.67–66.34	1.60–26.58
F <sub>Rn</sub> Mean (mBq m <sup>-2</sup> s <sup>-1</sup> )	10.25–128.03	5.44–26.35	0.90–140.33	9.07–152.38
C <sub>CO2</sub> Mean (%)	0.15–2.24	0.30–0.70	0.09–1.60	0.08–4.49
F <sub>CO2</sub> Mean (g m <sup>-2</sup> d <sup>-1</sup> )	7.59–70.51	71.00–175.84	9.98–53.79	12.48–254.69

old, and thick (approximately 200 km) lithospheric keel. They generally exhibit a low heat flow and a lack of volcanism and large earthquakes (King, 2005); examples include the Kaapvaal Craton, the North American Craton, and the Australian Craton. However, the NCC in eastern Asia is an exception. Recent studies have suggested that the eastern NCC had undergone significant lithospheric thinning and modification during the Mesozoic Cenozoic period, which was deduced by examining the physical and chemical properties of the subcontinental lithospheric mantle (Chen and Ai, 2009). The tectonic setting in the area is complex and comprises three grabens: the Linhe graben, the Yinchuan graben, and the Fenwei graben, and two main blocks: the Ordos block and the North China plain. It is a historically seismically active tectonic setting; along the numerous active faults up to 2020, 114 great earthquakes (with magnitudes of 6.0 to 8.5) occurred, 82 with magnitudes of 6.0 to 6.9, 23 of 7.0 to 7.9, and 9 of 8.0 to 8.5, respectively. These include the Haiyuan earthquake (M<sub>S</sub> = 8.5) in 1920 along the Haiyuan fault zone and the Tangshan earthquake (M<sub>S</sub> = 7.8) in 1976 along the Tangshan fault zone, followed by four aftershocks with magnitudes >6.0 (Fig. 1).

### 3. Sampling and analytical methods

The concentration and flux of Rn and CO<sub>2</sub> in soil gas were measured in the field along 100 profiles approximately perpendicular to the 52 faults (Fig. 1) from July to August 2018 and in May 2020. The measuring sites along the profile were at intervals of 5 to 40 m. The site intervals were 5 m near the fault scarps and gradually extended to the ends of the survey line away from the fault scarp, with a maximum interval distance of 40 m. The concentration measurement was taken at each measuring site along the profile across the fracture zones, the total number of the concentration measuring sites for each profile was 15, and the flux measurements were taken at the measuring sites within the fracture zones. The total number of flux measurement sites for each profile was 4. In total, the numbers of Rn concentrations and fluxes data were 1500 and 400, respectively, the same as those of CO<sub>2</sub> (Supplementary Data).

Soil gas Rn and CO<sub>2</sub> concentration measurements were taken by inserting a stainless-steel sampling tube with a diameter of 3 cm into the ground to a depth of 80 cm, which is fundamental for minimizing meteorological effects (Iskandar et al., 2004; Fujiyoshi et al., 2006), Rn and CO<sub>2</sub> fluxes were measured using a static closed chamber method. The instrument included an inverted, circular accumulation, hemispherical chamber with a volume of  $1.68 \times 10^{-2}$  m<sup>3</sup> and a radius of 0.2 m. The CO<sub>2</sub> concentration and flux were measured by a portable infrared CO<sub>2</sub> monitor (GXH-3010-E, Beijing HUAYUN Analytical Instrument Co., Ltd., Beijing, China). The detection limit and the measurement error of the monitor were 0.01 vol% and  $\pm 2$  vol%, respectively. The Rn concentration and flux measurements were taken in the field using a RAD 7 Rn detector (DURRIDGE, USA). Rn values were obtained 15 min after measuring (the time necessary for reaching <sup>218</sup>Po and <sup>222</sup>Rn nuclei

equilibrium, approximately 5 times the half-life of <sup>218</sup>Po). An inlet filter and a molecular sieve were used to protect the detector from dust and soil moisture. The detection limit and the measurement error of the RAD 7 were 14.8 Bq m<sup>-3</sup> and  $\pm 5\%$ , respectively.

Gas samples were collected by placing a cylindroid glass bottle (500 ml in volume, 0.5 cm in thickness, made of soda-lime glass) upside down. For spring gas sampling, the glass bottle was pre-filled with spring water attained from each sampling site and connected with a rubber tube to an inverted funnel fully sunk into the spring (Zhang et al., 2016), for the soil-gas well sampling, the glass bottle was pre-filled with saturated brine and connected with a rubber tube to the outlet of the apparatus. Gas released from the springs and soil gas wells went through the tube and filled the soda-lime bottle by replacing the water inside, which was then sealed with solid trapezoidal rubber plugs and adhesive plaster on-site (Chen et al., 2020). Three duplicated gas samples were collected from each spring sampling site, which was analyzed for <sup>3</sup>He/<sup>4</sup>He, R/Ra, and <sup>4</sup>He/<sup>20</sup>Ne, respectively; four duplicated gas samples were collected from each soil gas sampling site, which was analyzed for <sup>3</sup>He/<sup>4</sup>He, R/Ra, <sup>4</sup>He/<sup>20</sup>Ne,  $\delta^{13}\text{C}_{\text{CO}_2}$ , He and H<sub>2</sub> concentrations, respectively, while two duplicated water samples were collected from each spring sampling site, samples were filtered on site through a 0.45- $\mu\text{m}$  membrane filter before collection in HDPE bottles and sealed with parafilm. The samples were analyzed in the Analytical Laboratory of the Beijing Research Institute of Uranium Geology. The <sup>3</sup>He/<sup>4</sup>He (reported as R/Ra, Ra =  $1.4 \times 10^{-6}$ ) and <sup>4</sup>He/<sup>20</sup>Ne were determined by a VG5400 mass spectrometer, with uncertainties of  $\pm 0.3\%$ . The carbon isotope  $\delta^{13}\text{C}_{\text{CO}_2}$  (V-PDB) values were determined by the MAT 253 plus stable isotope ratio mass spectrometer with uncertainties of  $\pm 0.3\%$ . The  $\delta\text{D}$  and  $\delta^{18}\text{O}$  compositions of the water samples were analyzed with a Picarro L1102 mass spectrometer (Picarro, USA); the errors were 0.5‰ for  $\delta\text{D}$  and 0.1‰ for  $\delta^{18}\text{O}$ , respectively. The He and H<sub>2</sub> concentrations of soil gas were measured by an Agilent 3000 Micro GC with an error of  $\pm 5\%$ .

### 4. Results

The statistical data on the concentrations and fluxes of Rn and CO<sub>2</sub> in soil gas from the main active fault zones are listed in Table 1. The specific data of the geochemical characteristic of soil gas are presented as (Supplementary Data); the data on the geochemical characteristic of springs within the active fault zones are listed in Table 2.

The mean concentrations of Rn in each soil gas survey line were in the range of 1.60 to 66.34 kBq m<sup>-3</sup>. The mean fluxes of Rn in each soil gas survey line were in the range of 0.90 to 152.38 mBq m<sup>-2</sup> s<sup>-1</sup>. The mean concentrations of CO<sub>2</sub> in each soil gas survey line ranged from 0.08 to 4.49%. The mean fluxes of CO<sub>2</sub> ranged from 7.59 to 254.69 g m<sup>-2</sup> d<sup>-1</sup>.

According to the results calculated by the relative frequency histogram method, >80% of the soil gas Rn concentration and flux values were above the background values of the soil gas Rn concentration (below 10.00 kBq m<sup>-3</sup>) and flux (below 20 mBq m<sup>-2</sup> s<sup>-1</sup>) in the NCC. Furthermore, 57.6% of the soil gas CO<sub>2</sub> concentration was above 0.5%, and 70.1% of the soil gas CO<sub>2</sub> flux was above the background value of soil gas CO<sub>2</sub> flux (below 20 g m<sup>-2</sup> d<sup>-1</sup>) in North China (Li et al., 2018).

The <sup>3</sup>He/<sup>4</sup>He and <sup>4</sup>He/<sup>20</sup>Ne of the 18 spring gas samples were in the ranges of  $1.34 \times 10^{-8}$ – $7.80 \times 10^{-7}$  and 11–3212, respectively, and the  $\delta\text{D}$  and  $\delta^{18}\text{O}$  ranged from  $-12.02$  to  $-8.02\%$  and  $-89.28$  to  $-60.20\%$ , respectively (Table 2). The He and H<sub>2</sub> concentrations of the 15 soil gas sampling sites were in the range of 7.30–18.01 ppm and 0.77–9.18 ppm, respectively, and the  $\delta^{13}\text{C}_{\text{CO}_2}$  (V-PDB), <sup>3</sup>He/<sup>4</sup>He (R/Ra), and <sup>4</sup>He/<sup>20</sup>Ne were in the ranges of  $-20.9 \sim -18.0\%$ , 0.52–1.02, and 0.28–0.52, respectively (Supplementary Data).

**Table 2**  
Geochemical characteristics of springs within the active fault zones in the NCC.

Region	Number	Spring	Longitude (°E)	Latitude (°E)	$\delta D$ (‰)	$\delta^{18}O$ (‰)	$^3He/^4He$	$^4He/^{20}Ne$	R/Ra	Rc/Ra	References
Northeastern Tibetan Plateau	No.01	QL	103.628	36.4552	-82.35	-9.12	$1.10 \times 10^{-8}$	1048	0.01	0.01	This study
	No.02	SJ	106.253	36.587	-87.90	-9.19	$1.03 \times 10^{-7}$	841	0.07	0.07	
	No.03	SJ1	106.252	36.587	-80.71	-9.42	$7.21 \times 10^{-8}$	1611	0.05	0.05	
	No.04	CSH	106.04	36.131	-79.40	-9.80	$9.89 \times 10^{-8}$	15	0.07	0.05	
	No.05	XKH	106.082	36.019	-75.50	-11.74	$3.12 \times 10^{-8}$	158	0.02	0.02	
	No.06	XKH1	106.083	36.018	-76.99	-9.41	$1.70 \times 10^{-8}$	313	0.01	0.01	
	No.07	WM	106.991	34.737	-75.27	-9.39	$7.33 \times 10^{-7}$	25	0.02	0.07	
	No.08	ZMM	106.992	34.736	-74.50	-9.44	$1.41 \times 10^{-8}$	110	0.01	0.01	
	No.09	PL	106.661	35.543	-	-	$5.80 \times 10^{-7}$	-	0.4	-	
	No.10	QS	106.133	34.749	-	-	$7.31 \times 10^{-8}$	-	0.05	-	
	No.11	LT	109.174	34.363	-80.00	-9.70	$3.86 \times 10^{-7}$	-	0.28	-	
	No.12	MQ	108.641	34.343	-90.00	-7.50	$8.99 \times 10^{-8}$	-	0.06	-	
	No.13	LTD	109.198	34.063	-99.00	-11.90	$1.24 \times 10^{-7}$	-	0.09	-	
	No.14	MXX	107.842	34.019	-82.00	-11.00	$1.34 \times 10^{-8}$	-	0.1	-	
	No.15	QSWQ	106.121	34.752	-	-	$6.08 \times 10^{-8}$	-	0.04	-	
	No.16	WS	104.824	34.679	-	-	$5.48 \times 10^{-8}$	-	0.04	-	
	No.17	TW	105.068	35.12	-	-	$2.84 \times 10^{-8}$	-	0.02	-	
	No.18	JZ	105.48	34.375	-	-	$4.04 \times 10^{-8}$	-	0.03	-	
	No.19	HYTT	113.938	39.407	-89.00	-11.28	$8.86 \times 10^{-7}$	188.65	0.62	0.62	
No.20	YXNQ	114.441	39.8	-74.50	-10.50	$2.79 \times 10^{-6}$	284.9	1.95	1.95		
No.21	SMF	114.588	40.209	-60.20	-8.02	$1.07 \times 10^{-8}$	185.52	0.2	0.2		
No.22	HHY	115.543	40.336	-89.28	-11.60	$1.34 \times 10^{-6}$	202.85	0.96	0.96		
Zhang-Bo seismic zone	No.23	DWKC	116.084	40.959	-87.60	-11.49	$6.84 \times 10^{-7}$	135.54	0.49	0.49	This study
	No.24	CCTQ	115.743	40.901	-89.17	-12.02	$5.57 \times 10^{-7}$	85.42	0.42	0.42	
	No.25	WLY	115.932	40.476	-85.98	-11.78	$2.84 \times 10^{-6}$	28.83	2.03	2.04	
	No.26	ZHTQ	117.761	40.206	-74.04	-10.32	$5.95 \times 10^{-7}$	41.81	0.42	0.42	
	No.27	BDWS	117.344	39.549	-73.48	-9.65	$6.84 \times 10^{-7}$	44.5	0.49	0.49	
	No.28	JDWQ	116.935	39.958	-78.88	-10.49	$2.30 \times 10^{-7}$	82.53	0.16	0.16	
	No.29	MSHL	105.854	38.028	-61.91	-8.91	-	-	-	-	
The other seismic zone	No.30	XKH	106.082	36.019	-67.92	-9.34	-	-	-	-	This study
	No.31	PLLH	106.671	35.547	-78.68	-11.18	-	-	-	-	
	No.32	QC	107.148	34.638	-61.91	-8.91	-	-	-	-	
	No.33	SJZ	106.992	34.737	-67.57	-9.64	-	-	-	-	
	No.34	XY	106.404	35.945	-83.02	-11.97	-	-	-	-	
	No.35	DYZ	106.39	35.463	-64.98	-9.56	-	-	-	-	
	No.36	HJQ	106.185	35.667	-72.81	-10.97	-	-	-	-	
	No.37	XSQ	105.602	36.504	-71.28	-10.61	-	-	-	-	
	No.38	HTDD	105.787	35.755	-76.54	-10.08	-	-	-	-	
	No.39	HYQ	105.878	36.083	-67.92	-9.34	-	-	-	-	
	No.40	SLT	106.401	35.425	-66.56	-9.86	-	-	-	-	
	No.41	BYS	106.254	35.612	-73.13	-11.56	-	-	-	-	
	No.42	PY	106.629	35.849	-76.97	-10.73	-	-	-	-	
	No.43	LCS	106.181	35.74	-69.14	-9.63	-	-	-	-	
	No.44	CSH	106.039	36.133	-74.69	-10.90	-	-	-	-	
	No.45	NTQ	105.201	37.463	-67.2	-8.57	-	-	-	-	

(continued on next page)

Table 2 (continued)

Region	Number	Spring	Longitude (°E)	Latitude (°E)	δD (‰)	δ <sup>18</sup> O (‰)	<sup>3</sup> He/ <sup>4</sup> He	<sup>4</sup> He/ <sup>20</sup> Ne	R/R <sub>a</sub>	R <sub>c</sub> /R <sub>a</sub>	References
	No.46	DQ	106.339	37.967	-68.13	-8.97	-	-	-	-	
	No.47	DSG	106.149	38.891	-68.59	-10.49	-	-	-	-	
	No.48	LQS	106.277	38.962	-69.95	-9.41	-	-	-	-	
	No.49	JQ	106.481	39.082	-83.27	-11.66	-	-	-	-	
	No.50	QLG1	106.987	39.855	-69.00	-9.91	-	-	-	-	
	No.51	HQC	109.333	40.731	-74.95	-11.28	-	-	-	-	
	No.52	DHB	109.406	40.726	-75.89	-11.36	-	-	-	-	
	No.53	XSZ	108.733	40.739	-65.9	-9.19	-	-	-	-	
	No.54	STS	109.135	41.118	-76.16	-10.16	-	-	-	-	
	No.55	XRM	108.661	41.536	-63.70	-8.92	-	-	-	-	
	No.56	YG	108.294	41.291	-67.54	-10.24	-	-	-	-	
	No.57	XLS	107.928	41.284	-63.60	-9.12	-	-	-	-	
	No.58	HLST	107.789	41.285	-58.28	-8.79	-	-	-	-	
	No.59	DSMW	107.041	41.131	-67.39	-9.16	-	-	-	-	
	No.60	ZCJ	113.369	40.284	-70.42	-9.38	-	-	-	-	
	No.61	DXQ	113.015	38.423	-73.63	-10.72	-	-	-	-	
	No.62	MSJ	112.547	36.697	-72.90	-10.37	-	-	-	-	
	No.63	XXJ	111.233	35.115	-71.88	-9.62	-	-	-	-	

n.d. stands for no data. R/R<sub>a</sub> is the measured <sup>3</sup>He/<sup>4</sup>He ratio divided by that of air (R<sub>a</sub> = 1.4 × 10<sup>-6</sup>). R<sub>c</sub>/R<sub>a</sub> is the air-corrected <sup>3</sup>He/<sup>4</sup>He ratio calculated using the method: R<sub>c</sub>/R<sub>a</sub> = [(R/R<sub>a</sub> × X) - 1]/(X-1), X = [(<sup>4</sup>He/<sup>20</sup>Ne)<sub>measured</sub>/(<sup>4</sup>He/<sup>20</sup>Ne)<sub>air</sub>] × β<sub>Ne</sub>/β<sub>He</sub>. β is the Bunsen solubility coefficient, which is the volume of gas absorbed per volume of water at the measured temperature when the partial pressure of the gas is 1 atm (Weiss, 1971), the average atmospheric temperature during the gas samples analysis was 15°C, and β<sub>Ne</sub>/β<sub>He</sub> was 1.21 at 15°C.

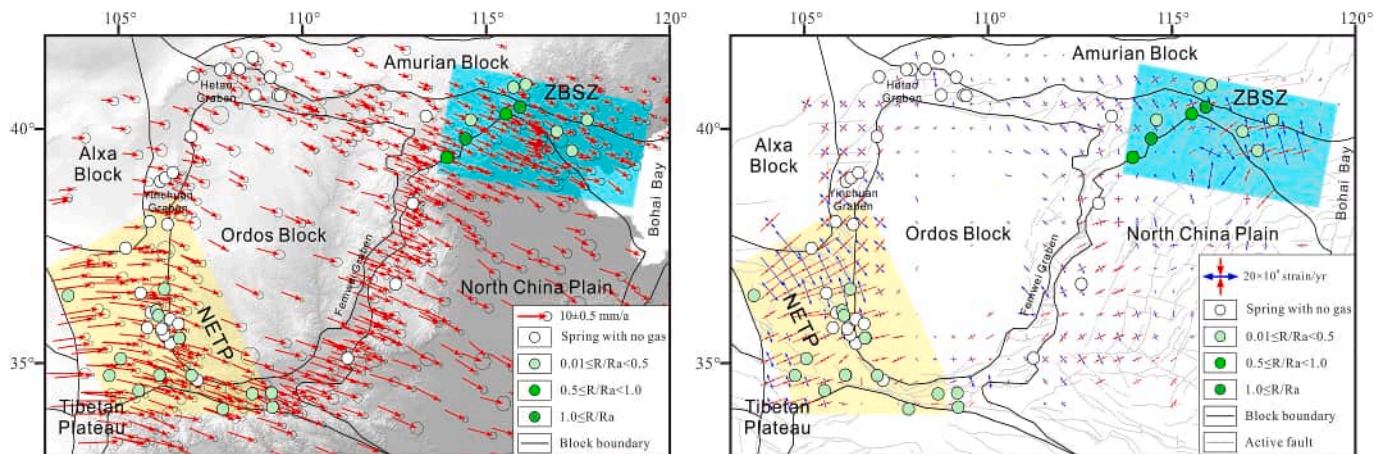


Fig. 2. <sup>3</sup>He/<sup>4</sup>He (R/R<sub>a</sub>) of gas samples from the springs in the study area. In particular: <sup>3</sup>He/<sup>4</sup>He and shear strain (a); <sup>3</sup>He/<sup>4</sup>He and GPS velocity (b); GPS velocity and shear strain data are according to Zhang et al. [2018] and Wang and Shen [2019].

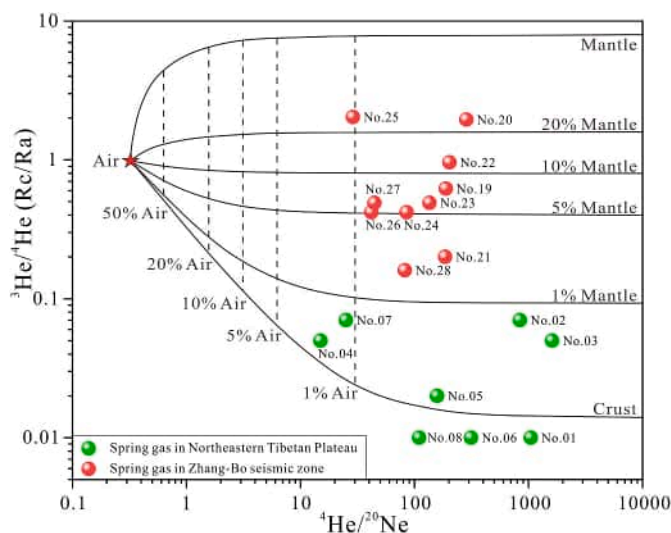


Fig. 3. <sup>3</sup>He/<sup>4</sup>He (R<sub>c</sub>/R<sub>a</sub>) versus <sup>4</sup>He/<sup>20</sup>Ne of gas samples from the springs in the study area.

## 5. Discussion

### 5.1. Spatial distribution of gas geochemistry in the fault zones of the NCC

Among the 63 springs within the fault zones of the NCC, gas sampling was achieved in only 28 springs distributed in the NETP and the ZBSZ. Gas sampling was failed in the other seismic zone, where no visible gas was found in the 35 springs. The <sup>3</sup>He/<sup>4</sup>He ratios (R/R<sub>a</sub>) of the gas sampled in the 28 springs ranged from 0.01 to 2.03, which ranged from 0.01 to 0.40 in the 18 springs in the NETP, and from 0.16 to 2.03 in the 10 springs in the ZBSZ (Fig. 2). In addition, it was shown in the <sup>3</sup>He/<sup>4</sup>He (R/R<sub>a</sub>)-<sup>4</sup>He/<sup>20</sup>Ne diagram that the points of the 8 springs in the NETP were all distributed in the crust-derived component, while all of the points of the 10 springs in the ZBSZ obviously jumped upward the mantle-derived component (Fig. 3). Based on the spatial distribution of the <sup>3</sup>He/<sup>4</sup>He (R/R<sub>a</sub>)-<sup>4</sup>He/<sup>20</sup>Ne of gas samples from the 28 springs, it could be roughly inferred that crust-derived gas dominated the gas from the 8 springs in the NETP, while both crust-derived and mantle-derived gas could be significant contributors for the gas from the 10 springs in the ZBSZ.

In addition, high soil gas R<sub>n</sub> and CO<sub>2</sub> emissions have been observed

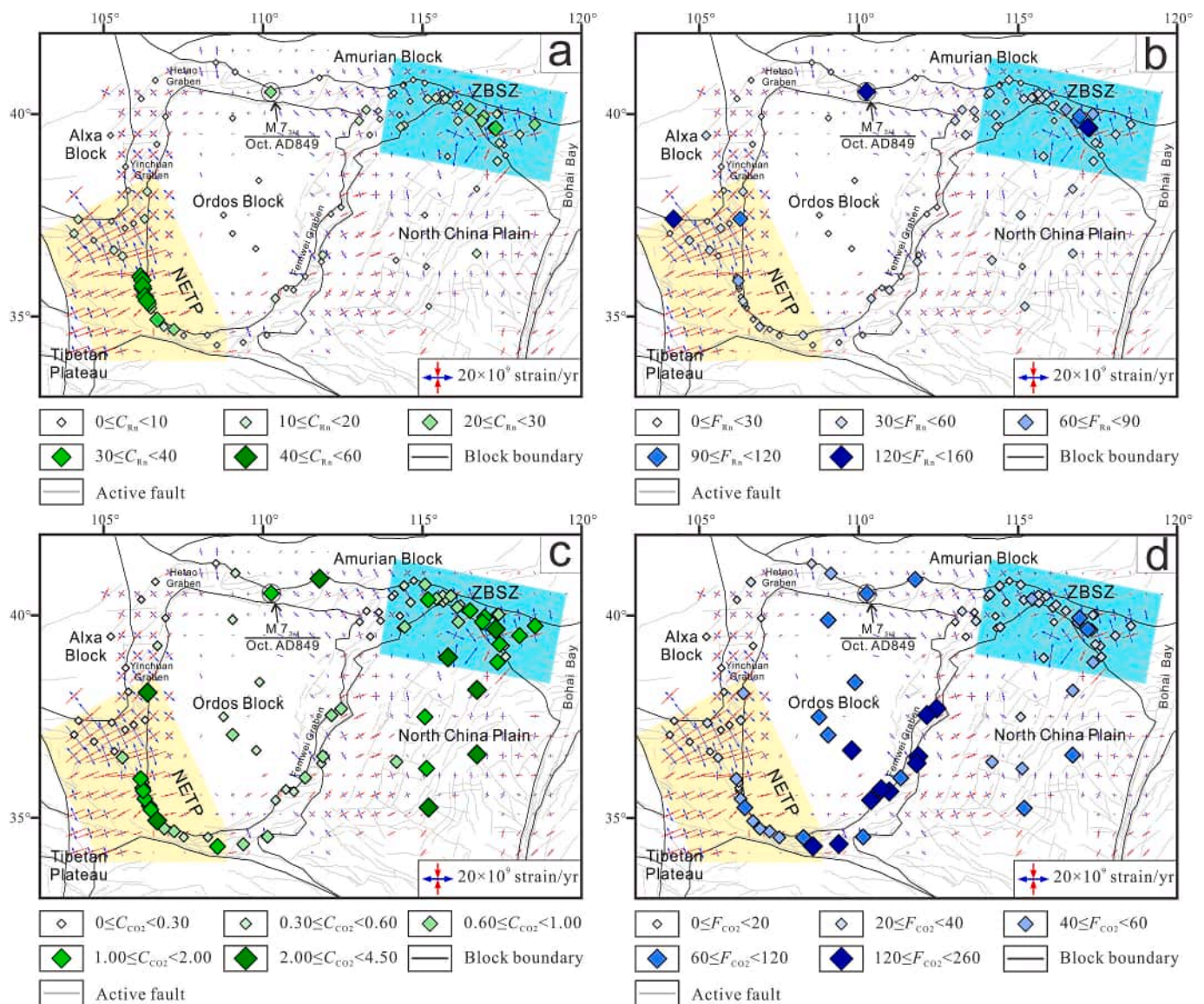


**Fig. 4.** Soil gas degassing features in the NCC. In particular: (a) Rn concentration and shear strain; (b) Rn flux and shear strain; (c) CO<sub>2</sub> concentration and shear strain; (d) CO<sub>2</sub> flux and shear strain. Shear strain data are according to Zhang et al. [2018] and Wang and Shen [2019]. The yellow zone is the ZBSZ, the blue zone is the NETP. (For interpretation of the references to colour in this figure legend, the reader is referred to the web version of this article.)

in active fault zones in the NETP and the ZBSZ (Figs. 4 and 5). The mean Rn concentration and flux from the active fault zones in the NETP ( $4.67\text{--}66.34 \text{ kBq m}^{-3}$  and  $0.90\text{--}140.33 \text{ mBq m}^{-2} \text{ s}^{-1}$ ) and the ZBSZ ( $3.80\text{--}37.89 \text{ kBq m}^{-3}$  and  $10.25\text{--}152.38 \text{ mBq m}^{-2} \text{ s}^{-1}$ ) were much higher than those in the other fault zones in the study area ( $1.60\text{--}15.33 \text{ kBq m}^{-3}$  and  $3.66\text{--}49.82 \text{ mBq m}^{-2} \text{ s}^{-1}$ ) and the Ordos basin ( $0.20\text{--}8.35 \text{ kBq m}^{-3}$  and  $0.10\text{--}26.35 \text{ mBq m}^{-2} \text{ s}^{-1}$ ). The average values of Rn concentration and flux in the NETP ( $23.55 \text{ kBq m}^{-3}$  and  $32.69 \text{ mBq m}^{-2} \text{ s}^{-1}$ ) were 3.4 and 1.2 times as high as those in the other fault zones, except for those in the ZBSZ, and 4.4 and 1.9 times as high as those in the Ordos Basin. The average values of Rn concentration and flux in the ZBSZ ( $13.18 \text{ kBq m}^{-3}$  and  $47.64 \text{ mBq m}^{-2} \text{ s}^{-1}$ ) were 1.9 and 1.7 times as high as those in the other fault zones, except for those in the NETP, and 2.5 and 2.7 times as high as those in the Ordos basin (Table 1). Also, a high CO<sub>2</sub> concentration and flux were observed in the NETP and the ZBSZ, although the high CO<sub>2</sub> concentration and flux were partially distributed in the other fault zone and the Ordos Basin. In particular, both concentrations and fluxes of Rn and CO<sub>2</sub> were high in the soil gas profile ADL, where significant earthquakes occurred ([http://news.ceic.](http://news.ceic.ac.cn)

[ac.cn](http://news.ceic.ac.cn)), such as the Baotou M<sub>s</sub> 6.4 earthquake in May 1996 and M<sub>s</sub> 7.8 earthquake in 849 (Dong et al., 2018). Therefore, the high concentrations and fluxes of Rn and CO<sub>2</sub> in soil gas profile ADL might be attributed to the relatively high crustal permeability likely induced by strong seismic events (Chen et al., 2018).

The natural radioactive decay of <sup>226</sup>Ra is a unique source of soil gas <sup>222</sup>Rn. Whereas soil gas CO<sub>2</sub> is derived from multiple sources, it primarily originates from mantle degassing, carbonate metamorphism, carbonated dissolution, the decomposition of organic matter, and soil respiration (Caudron et al., 2012; Rannarine et al., 2012). In the  $\delta^{13}\text{C}_{CO_2}$  vs.  $1/CO_2$  diagram, the soil gas samples plotted within the composition mixing range between the Deep (M + C) end-member and biogenic end-member (Fig. 6), in accordance with the relatively high He concentrations ( $7.30\text{--}18.01 \text{ ppm}$ ) and strong relation between soil gas CO<sub>2</sub> and He concentrations (Fig. 7), geological CO<sub>2</sub> could be inferred to ascend toward the surface through the faults in the ZBSZ, which could play a role as the carrier of geological Rn and transferred it to the shallower soil gas. In the NETP, the He concentration of soil gas within the fault zones reached up to  $65.30 \text{ ppm}$  (Zhou et al., 2011), in

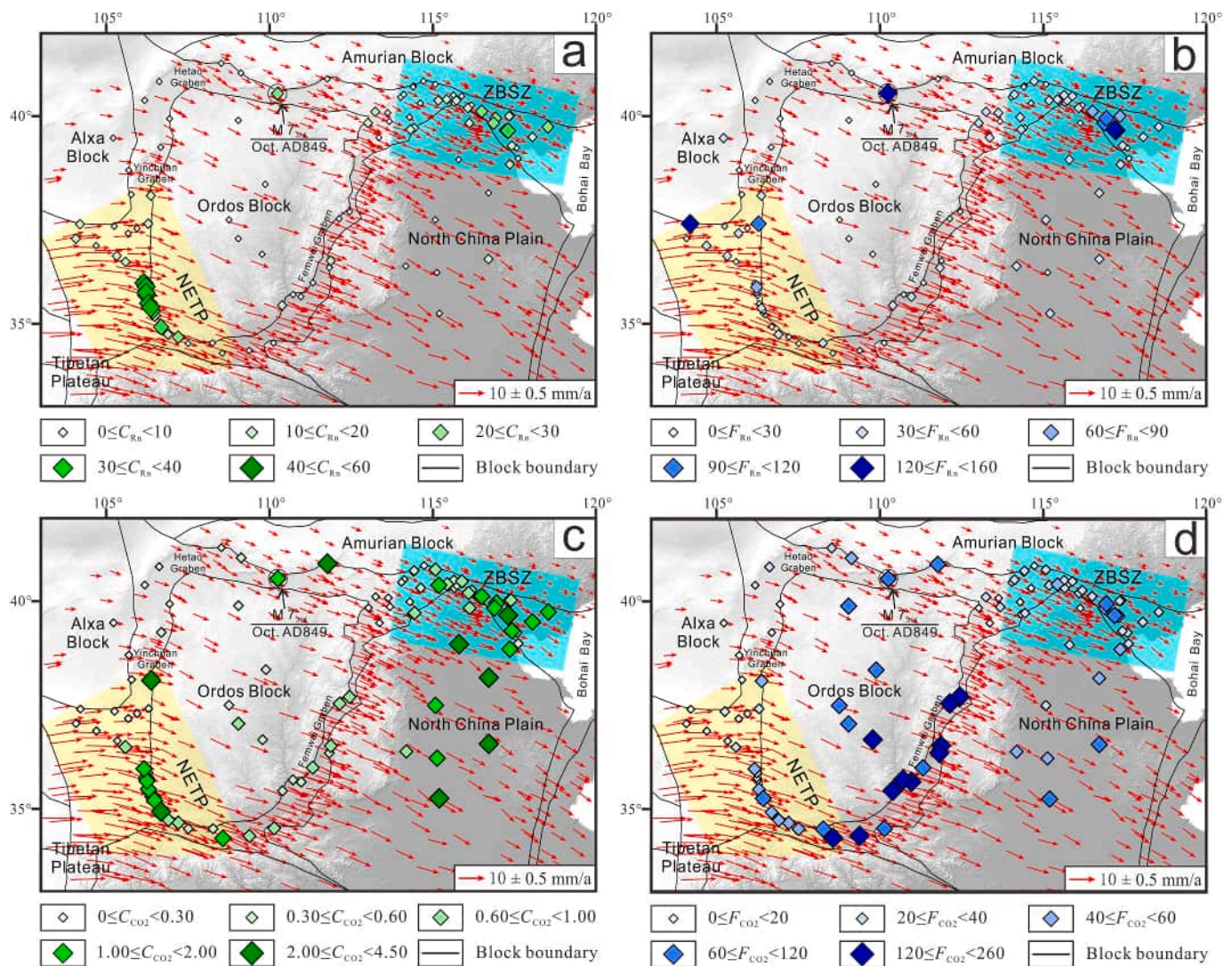


**Fig. 5.** The soil gas degassing features in the NCC. In particular: (a) Rn concentration and GPS velocity; (b) Rn flux and GPS velocity; (c) CO<sub>2</sub> concentration and GPS velocity; (d) CO<sub>2</sub> flux and GPS velocity. GPS velocity data are according to Zhang et al. [2018] and Wang and Shen [2019]. The yellow zone is the ZBSZ, the blue zone is the NETP. (For interpretation of the references to colour in this figure legend, the reader is referred to the web version of this article.)

accordance with the strong relationship between soil gas CO<sub>2</sub> and Rn concentrations (Fig. 7), the geological source for soil gas within the fault zones could also be inferred.

Therefore, it was apparent that the relatively high gas emissions from the fault zones, including geological gas in the soil gas and deep-derived gas (crust or mantle-derived gases) from springs, showed a concentrated distribution in the NETP and the ZBSZ. It suggested that a particular tectonic framework could be responsible for the coupled spatial distribution of gas geochemistry in the fault zones of the NCC.

## 5.2. Tectonic framework in the NCC revealed by fluid geochemistry

Although a coupled concentrated distribution of the degassing for geological soil gas and deep-derived gas (crust or mantle-derived gases) from springs were observed within the fault zone in the NCC, pronounced differences were still found between the isotopic ratios of gas from the springs within the NETP and those within the ZBSZ, according to the <sup>3</sup>He/<sup>4</sup>He (R/Ra) and <sup>4</sup>He/<sup>20</sup>Ne of gas from the springs. It seemed that abundant mantle-derived gas was degassing through the fault in the ZBSZ, while a minute amount of mantle-derived gas was degassing in the NETP (Fig. 3).

Previous research has suggested that the joint action of the India-

Eurasia collision and the Pacific subduction could be a significant factor that dominated the tectonic evolution in the NCC (Chen and Ai, 2009). Due to the remote action of the India-Eurasia collision, the Tibetan Plateau moved northeastward; that movement was withstood when the Tibetan Plateau collided with the rigid Ordos block in the northeastern corner of the Tibetan Plateau. Crust shortening and over thrusting in the northeastern corner occurred (Lease et al., 2011), resulting in strong tectonic compression in the NETP margin (Fig. 1). Due to the continuous subduction and rollback of the Pacific plate, lithosphere consumption and intense lithosphere regional extension took place in the eastern NCC. This caused the eastward motion of the North China plain (Zeng et al., 2016) and obvious GPS velocity differences between the North China plain and the Amurian block, resulting in the strike-slip characteristic of the ZBSZ (Zhang et al., 2018; Wang and Shen, 2019).

In fact, extensional tectonics have been verified to facilitate fracture development, causing a stronger degassing in the normal fault zones than the thrust and strike-slip faults (Tamburello et al., 2018). Therefore, the degassing from the fault zones in the NETP and the ZBSZ should be weaker than those in the other tectonic belts in the NCC. This could be attributed to the widespread thrust and strike-slip faults in the NETP and the dominant strike-slip in the ZBSZ, whereas normal faults dominate in

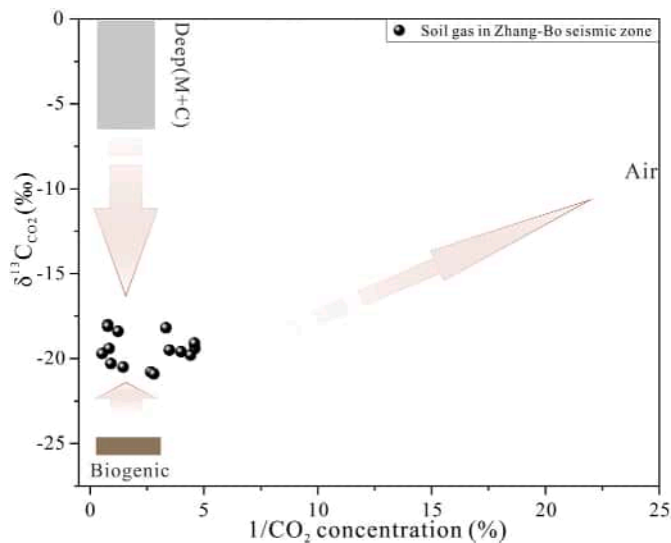


Fig. 6. Plot showing  $\delta^{13}\text{C}_{\text{CO}_2}$  vs.  $1/\text{CO}_2$  values for gas samples from the soil gas wells and springs. Deep (M + C): end-member of mantle and crust sources, biogenic: end-member of biogenic source, Air: end-member of the atmospheric source.

the other tectonic belts (Fig. 1). Unexpectedly, relative to those in the other tectonic belts, high soil gas Rn and  $\text{CO}_2$  emissions were observed (Figs. 4 and 5), and degassing in the springs only occurred in the NETP and the ZBSZ (Figs. 4 and 5).

By coincidence, an abnormally high shear strain rate and the steepest gradient of GPS horizontal velocity were also observed in the NETP and the ZBSZ (Figs. 4 and 5). The abnormal regions were roughly consistent with those where high geological soil gas (Rn,  $\text{CO}_2$  and He) emission and deep-derived gas (crust or mantle-derived gases) exhalation from springs were observed (Figs. 2–5 and 7). Furthermore, it has been found in previous simulation experiments that substantially enhanced gas emissions from rocks could happen, when the differential stress on the rocks exceeded their compressive strength, resulting in the development of macroscopic fractures (new fracturing or an opening of preexisting fractures), which provides new pathways for captive gas in the rocks (Roeloffs, 1999; Girault et al., 2017). Therefore, based on the above discussion, it could be inferred that fracture development in the deep earth beneath the NETP and the ZBSZ might have occurred because of the strong regional tectonic activity there, leading to enhanced gas

exhalation from the rocks in the deep earth. That might in turn have led to more gas emissions and a larger contribution of geological soil gas and deep-derived gas from springs in the NETP and the ZBSZ than those in the other seismic zones (Figs. 2–7).

In addition, the low-velocity zones 20–40 km depth were outlined beneath both the NETP and the ZBSZ (Wang et al., 2009; Zhao et al., 2021). In the ZBSZ where strike-slip and normal deep faults dominate the tectonic zone, the low-velocity zone was sketchily outlined as a mantle-derived intrusion into the crust by geophysical research (Huang and Zhao, 2005; Wang et al., 2009; Wu et al., 2021), in coordination with the abundant mantle-derived gas observed in the springs along the faults in the ZBSZ in this study, the mantle-derived intrusion into the crust beneath the ZBSZ could be further confirmed, and mantle-derived gas trapped within the intrusion could have ascended toward the surface through deep faults in the ZBSZ. Also, the development of new fractures within the fault zone could have facilitated the migration of trapped mantle-derived gas in the ZBSZ (Fig. 8b). Meanwhile, the low-velocity zone beneath the NETP was proven by various geophysical means to be a channel flow (Royden et al., 1997; Clark and Royden, 2000), flowing eastward along the decollement plane (Jiang et al., 2014; Du et al., 2018), which were intersected by deep-cut DBF, WQLF, and LPSF (Fig. 8a). In addition, larger magnitudes of  $\delta^{18}\text{O}$  shift for water samples in the NETP than those in the ZBSZ have been observed (Fig. 9). It is recognized that rocks are rich in oxygen (>40%) and poor in hydrogen (<1%) (Craig, 1961), the occurrence of reactions between water and rocks can result in an oxygen shift in water, whereas  $\delta\text{D}$  remains largely stable (Skelton et al., 2014). Therefore, the obvious  $\delta^{18}\text{O}$  shift could be additional evidence for more new fractures in the NETP than in the ZBSZ, on the basis that enhanced water-rock interaction on the new surface of rocks could increase  $\delta^{18}\text{O}$  shift (Chen et al., 2015). That could indicate that more new fractures occurred in the NETP than that in the ZBSZ, and more pathways for gas propagation were created there, subject to the more substantial compressional deformation, and higher shear strain in the NETP (Figs. 4 and 5), the alternative distribution of high-resistivity and low-resistivity beneath the NETP also implied that the crust was highly broken in the NETP (Zhan et al., 2017). Although more new fractures have been proved to be developed in the NETP than those in the ZBSZ, negligible mantle-derived gas was detected in springs in these faults (Fig. 2), which suggested that the low-velocity zone beneath the NETP could be purely crust-derived. Thus, our research suggested that the channel flow beneath the NETP might form within the crust, with the probable leading front reaching the LPSF (Fig. 8a), where an indeterminate image for the channel flow had been shown (Zhao et al., 2021).

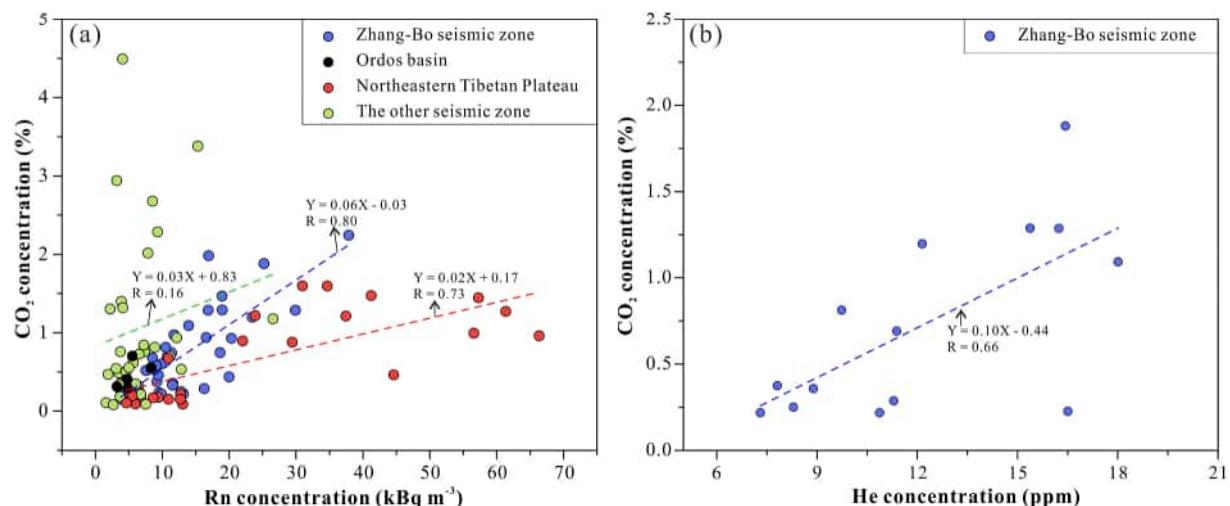
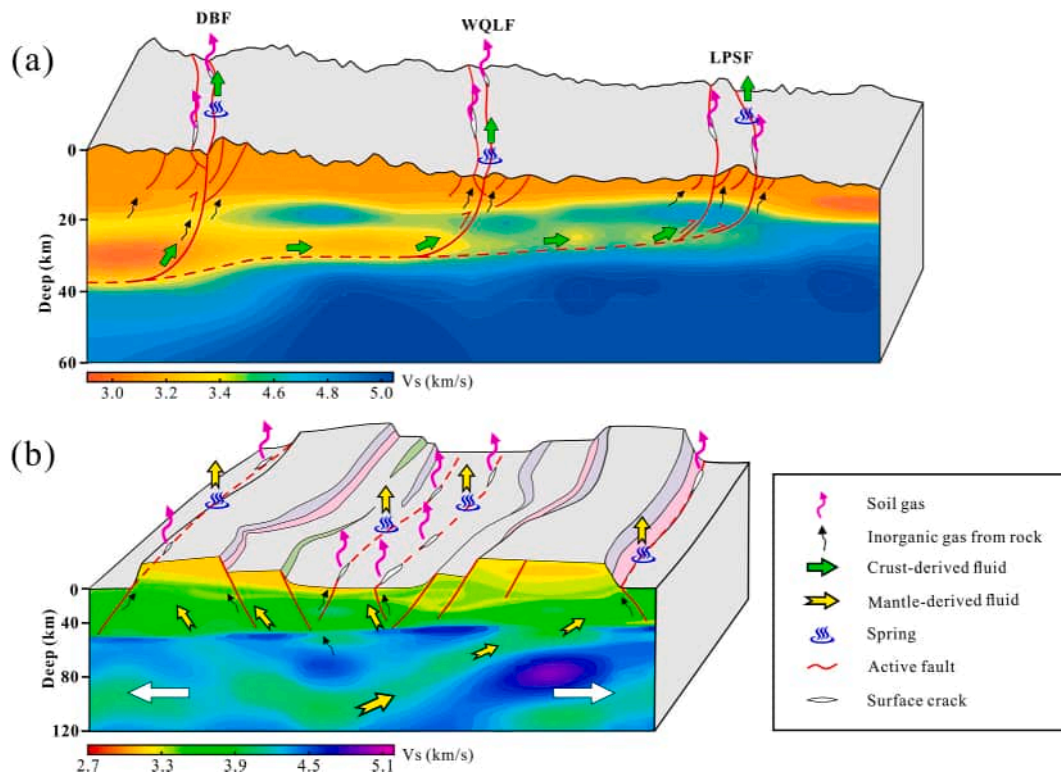
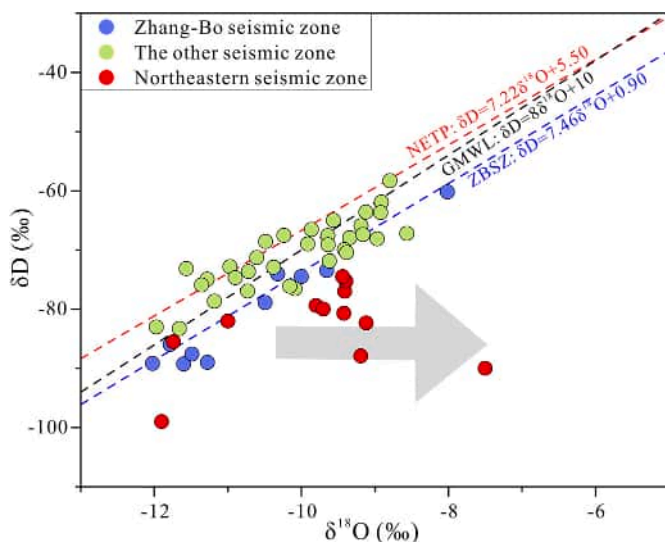


Fig. 7. Relation between soil gas concentrations in the NCC. (a): Rn and  $\text{CO}_2$  concentrations in the NCC. (b) He and  $\text{CO}_2$  concentrations in the ZBSZ.



**Fig. 8.** Conceptual model for the difference of gas geochemistry between the NETP and the ZBSZ. (a) Conceptual model for the NETP. (b) Conceptual model for the ZBSZ. (The low-velocity zones are according to Wang et al., 2009 and Zhao et al., 2021; the fault zones are according to Jiang and Zhang, 2012 and Du et al., 2018.)



**Fig. 9.**  $\delta D$  versus  $\delta^{18}O$  of water samples from the springs in the study area. GMWL stands for global meteoric water line:  $\delta D = 8 \delta^{18}O + 10$  (Craig, 1961); NETP stands for local meteoric water line in the NETP:  $\delta D = 7.22 \delta^{18}O + 5.50$  (Sun et al., 2016b); ZBSZ stands for local meteoric water line in the ZBSZ:  $\delta D = 7.46 \delta^{18}O + 0.90$  (Liu et al., 2010).

**6. Conclusions**

By means of a comprehensive analysis of the distribution of geochemical characteristics of fluids and geophysical characteristics within the principal active fault zones in the NCC, three conclusions can be summarized as follows:

(1) Obvious high Rn and slightly high CO<sub>2</sub> and He emissions were observed in active fault zones in the NETP, which is dominated by strong

compression and thrust faults, and in the ZBSZ, which is dominated by regional extension and strike-slip fault, while Rn and CO<sub>2</sub> emissions were higher than those in the other tectonic belts with dominant extensions and normal faults in the NCC. It goes against previous research proposed that gas emissions in extensional tectonics and normal faults could be stronger than those in compression tectonics, thrust faults, and strike-slip faults.

(2) It was apparent that relatively high gas emissions from fault zones, including geological gas in soil gas and deep-derived gas (crust or mantle-derived gases) from springs, showed a concentrated distribution in the NETP and the ZBSZ. Also, an abnormally high shear strain rate and the steepest gradient of GPS horizontal velocity were both observed in the NETP and the ZBSZ. This suggests that fractures in the deep earth beneath the NETP and the ZBSZ might have developed under the strong regional tectonic activity there. This might have resulted in greater contributions of geological soil gas and deep-derived gas from springs in the NETP and the ZBSZ than those presented in the other seismic zones.

(3) The comprehensive analysis confirmed the mantle-derived intrusion into the crust beneath the ZBSZ, and the development of new fractures within the fault zone could have facilitated the migration of trapped mantle-derived gas in the ZBSZ. However, the channel flow beneath the NETP, shown by the low-velocity zone 20 to 40 km deep, intersected by deep-cut faults, could have formed within the crust, since negligible mantle-derived gas was detected in the springs in the NETP, even if more new fractures have been proved to be developed there.

(4) Based on the distribution of the geochemical characteristics of the fluid within the principal active fault zones in the NCC, it could be inferred that stronger regional tectonic activity might have occurred in the NETP and the ZBSZ than the other seismic zones, which suggested that more attention should be paid to the potential of future seismogenesis in the NETP and ZBSZ, and gas geochemistry could be a preferential method for monitoring regional tectonic and seismic activity.

## Declaration of Competing Interest

None.

## Data availability

All the data have been deposited in Mendeley Data repository (Mendeley Data, V2, doi: 10.17632/5bnvwxmtv8.2).

## Acknowledgements

This study was jointly supported by the National Key Research and Development Program of China (No. 2019YFC1509203), Natural Science Foundation of China (Nos. 41402298, 42073063), the Basic Science Research Plan of the Institute of Earthquake Science, China Earthquake Administration (No.2020IEF0704, 2021IEF0707, and 2021IEF1205), this work is a contribution to IGC Project 724. Research data associated with this article had been uploaded to Mendeley Data (<https://data.mendeley.com/drafts/k7xf85nr2>). All the data have been deposited in Mendeley Data repository (Chen, Zhi (2022), “Tectonic features of the Tibetan Plateau–Ordos Block contact zone (central northern China) from gas geochemistry and seismic imaging”, Mendeley Data, V2, doi: <https://doi.org/10.17632/5bnvwxmtv8.2>).

## Appendix A. Supplementary data

Supplementary data to this article can be found online at <https://doi.org/10.1016/j.chemgeo.2022.121048>.

## References

- Bedrosian, P., Unsworth, M., Egbert, G., Thurber, C.H., 2004. Geophysical images of the creeping segment of the San Andreas fault: implications for the role of crustal fluids in the earthquake process. *Tectonophysics* 385 (1–4), 137–158. <https://doi.org/10.1016/j.tecto.2004.02.010>.
- Bonforte, A., Federico, C., Giammanco, S., Guglielmino, F., Liuzzo, M., Neria, M., 2013. Soil gases and SAR measurements reveal hidden faults on the sliding flank of Mt. Etna (Italy). *J. Volcanol. Geotherm. Res.* 251, 27–40. <https://doi.org/10.1016/j.jvolgeores.2012.08.010>.
- Caudron, C., Mazot, A., Bernard, A., 2012. Carbon dioxide dynamics in Kelud volcanic lake. *J. Geophys. Res.-Solid Earth* 117, B05102. <https://doi.org/10.1029/2011JB008806>.
- Chen, L., Ai, Y.S., 2009. Discontinuity structure of the mantle transition zone beneath the North China Craton from receiver function migration. *J. Geophys. Res.-Solid Earth* 114, B06307. <https://doi.org/10.1029/2008JB006221>.
- Chen, B., Tian, W., Zhai, M., 2005. Zircon U-Pb geochronology and geochemistry of the Mesozoic magmatism in the Taihang Mountains and other places of the North China craton, with implications for petrogenesis and geodynamic setting. *Acta Petrol. Sin.* 21 (1), 13–24. <https://doi.org/10.1016/j.sedgeo.2003.12.012>.
- Chen, L., Jiang, M., Yang, J., Wei, Z., Liu, C., Ling, Y., 2014. Presence of an intralithospheric discontinuity in the central and western North China Craton: implications for destruction of the craton. *Geology* 42 (3), 223–226. <https://doi.org/10.1130/G35010.1>.
- Chen, Z., Wang, X., Wang, J., Hang, Y., 2015. Highly transparent terbium gallium garnet crystal fabricated by the floating zone method for visible–infrared optical isolators. *Opt. Mater.* 46, 12–15. <https://doi.org/10.1016/j.optmat.2015.03.034>.
- Chen, Z., Li, Y., Liu, Z., Wang, J., Zhou, X., Du, J., 2018. Radon emission from soil gases in the active fault zones in the Capital of China and its environmental effects. *Sci. Rep.* 8, 16772. <https://doi.org/10.1038/s41598-018-35262-1>.
- Chen, Z., Li, Y., Liu, Z., Zheng, G., Xu, W., Yan, W., Yi, L., 2019. CH<sub>4</sub> and CO<sub>2</sub> emissions from mud volcanoes on the southern margin of the Junggar Basin, NW China: Origin, output, and relation to regional tectonics. *J. Geophys. Res.-Solid Earth* 124 (5), 5030–5044. <https://doi.org/10.1029/2018JB016822>.
- Chen, Z., Li, Y., Martinelli, G., Liu, Z., Lu, C., Zhao, Y., 2020. Spatial and temporal variations of CO<sub>2</sub> emissions from the active fault zones in the capital area of China. *Appl. Geochem.* 112, 104489. <https://doi.org/10.1016/j.apgeochem.2019.104489>.
- Clark, M., Royden, L., 2000. Topographic ooze: building the eastern margin of Tibet by lower crustal flow. *Geology* 28 (8), 703–706. [https://doi.org/10.1130/0091-7613\(2000\)28<703:TOBTEM>2.0.CO;2](https://doi.org/10.1130/0091-7613(2000)28<703:TOBTEM>2.0.CO;2).
- Craig, H., 1961. Isotopic variations in meteoric waters. *Science* 133 (3465), 1702–1703. <https://doi.org/10.1126/Science.133.3465.1702>.
- Crossey, L.J., Karlstrom, K.E., Springer, A.E., Newell, D., Hilton, D.R., Fischer, T., 2009. Degassing of mantle-derived CO<sub>2</sub> and <sup>3</sup>He from springs in the southern Colorado Plateau region—flux rates, neotectonics connections, and implications for understanding the groundwater system. *Geol. Soc. Am. Bull.* 121, 1034–1053. <https://doi.org/10.1130/B26394.1>.
- D’Alessandro, A., Scudero, S., Sino, M., Alessandro, G., Mineo, R., 2020. Long-Term monitoring and characterization of soil radon emission in a seismically active area. *Geochem. Geophys. Geosyst.* 21. <https://doi.org/10.1029/2020GC009061>.
- Dong, S., Zhang, P., Zheng, W., Yu, Z., Lei, Q., Yang, H., Liu, J., Gong, H., 2018. Paleoseismic observations along the Langshan range-front fault, Hetao Basin, China: Tectonic and seismic implications. *Tectonophysics* 730, 63–80. <https://doi.org/10.1016/j.tecto.2018.02.012>.
- Du, F., Wen, X., Feng, J., Liang, M., Long, F., Jiang, W., 2018. Seismo-tectonics and seismic potential of the Liupanshan fault zone (LPSEZ), China. *Chin. J. Geophys.-Chin. Ed.* 61 (2), 545–559. <https://doi.org/10.6038/cjg2018L0181> (in Chinese with an English abstract).
- Faulkner, D.R., Jackson, C.A.L., Lunn, R.J., Schlische, R.W., Shipton, Z.K., Wibberley, C. A.J., Withjack, M.O., 2010. A review of recent developments concerning the structure, mechanics and fluid flow properties of fault zones. *J. Struct. Geol.* 32, 1557–1575. <https://doi.org/10.1016/j.jsg.2010.06.009>.
- Fujiyoshi, R., Sakamoto, K., Imanishi, T., Sumiyoshi, T., Sawamura, S., Vaupotic, J., Kobal, I., 2006. Meteorological parameters contributing to variability in <sup>222</sup>Rn activity concentrations in soil gas at a site in Sapporo, Japan. *Sci. Total Environ.* 370 (1), 224–234. <https://doi.org/10.1016/j.scitotenv.2006.07.007>.
- Girault, F., Schubnel, A., Pili, É., 2017. Transient radon signals driven by fluid pressure pulse, micro-crack closure, and failure during granite deformation experiments. *Earth Planet. Sci. Lett.* 474 (15), 409–418. <https://doi.org/10.1016/j.epsl.2017.07.013>.
- He, H., Zhu, R., Saxton, J., 2011. Noble gas isotopes in corundum and peridotite xenoliths from the eastern North China Craton: implication for comprehensive refertilization of Lithospheric mantle. *Phys. Earth Planet. Inter.* 189 (3–4), 185–191. <https://doi.org/10.1016/j.pepi.2011.09.001>.
- Huang, J., Zhao, D., 2005. Fine structure of three dimensional P-wave velocity beneath the capital region and deep environment for the nucleation of strong earthquakes. *Chin. Sci. Bull. (Chin. Ver.)* 50 (6), 544–552. <https://doi.org/10.3321/j.issn:0023-074X.2005.04.009> (in Chinese with an English abstract).
- Iskandar, D., Yamazawa, H., Iida, T., 2004. Quantification of the dependency of radon emanation power on soil temperature. *Appl. Radiat. Isot.* 60 (6), 971–973. <https://doi.org/10.1016/j.apradiso.2004.02.003>.
- Jiang, W.L., Zhang, J.F., 2012. Fine crustal structure beneath Capital area of China derived from gravity. *Chin. J. Geophys.-Chin. Ed.* 55 (5), 1646–1661. <https://doi.org/10.6038/j.issn.0001-5733.2012.05.022> (in Chinese with an English abstract).
- Jiang, C., Yang, Y., Zheng, Y., 2014. Penetration of mid-crustal low velocity zone across the Kunlun fault in the NE Tibetan plateau revealed by ambient noise tomography. *Earth Planet. Sci. Lett.* 406, 81–92. <https://doi.org/10.1016/j.epsl.2014.08.040>.
- King, S.D., 2005. Archean cratons and mantle dynamics. *Earth Planet. Sci. Lett.* 234 (1–2), 1–14. <https://doi.org/10.1016/j.epsl.2005.03.007>.
- Koike, K., Yoshinaga, T., Suetsugu, K., Kashiwaya, K., Asaue, H., 2015. Controls on radon emission from granite as evidenced by compression testing to failure. *Geophys. J. Int.* 203 (1), 428–436. <https://doi.org/10.1093/gji/ggv290>.
- Lease, R.O., Burbank, D.W., Clark, M.K., Farley, K.A., Zheng, D.W., Zhang, H.P., 2011. Middle Miocene reorganization of deformation along the northeastern Tibetan Plateau. *Geology* 39 (4), 359–362. <https://doi.org/10.1130/G31356.1>.
- Li, J., Chen, Z., Lu, L.N., Zhou, X.C., Li, Y., 2018. Degassing of CO<sub>2</sub>, Rn and Hg from the Xiadian Active Fault and their environmental significance. *Bull. Mineral. Petrol. Geochem.* 37 (4), 629–638 (in Chinese with an English abstract).
- Liu, J.R., Song, X.F., Yuan, G.F., Sun, X.M., Liu, X., Wang, S.Q., 2010. Characteristics of δ<sup>18</sup>O in precipitation over Eastern Monsoon China and the water vapor sources. *Chin. Sci. Bull. (Chin. Ver.)* 55 (2), 200–211. <https://doi.org/10.1007/s11434-009-0202-7>.
- Lu, C., Li, Y., Chen, Z., Liu, Z., Zhao, Y., Hu, L., 2021. Fluid geochemistry within the north China Craton: spatial variation and genesis. *Geofluids* 2021, 1009766. <https://doi.org/10.1155/2021/1009766>.
- Martinelli, G., Tamburello, G., 2020. Geological and geophysical factors constraining the occurrence of earthquake precursors in geofluids: a review and reinterpretation. *Front. Earth Sci.* 8, 596050. <https://doi.org/10.3389/feart.2020.596050>.
- Muirhead, J.D., Fischer, T.P., Oliva, S.J., Laizer, A., van Wijk, J., Currie, C.A., Lee, H., Judd, E.J., Kazimoto, E., Sano, Y., Takahata, N., Tiberi, C., Foley, S.F., Dufek, J., Reiss, M.C., Ebinger, C.J., 2020. Displaced cratonic mantle concentrates deep carbon during continental rifting. *Nature* 582 (7810), 67–72. <https://doi.org/10.1038/s41586-020-2328-3>.
- Neri, M., Ferrara, E., Giammanco, S., Currenti, G., Cirrincione, R., Patané, G., Zanon, V., 2016. Soil radon measurements as a potential tracer of tectonic and volcanic activity. *Sci. Rep.* 6 (1), 24581. <https://doi.org/10.1038/srep24581>.
- Pang, J., Pang, Z., Lv, M., Tian, J., Kong, Y., 2018. Geochemical and isotopic characteristics of fluids in the Niutuozhen geothermal field, North China. *Environ. Earth Sci.* 77 (1), 12. <https://doi.org/10.1007/s12665-017-7171-y>.
- Perchuk, A.L., Gerya, T.V., Zakharov, V.S., Griffin, W.L., 2020. Building cratonic keels in Precambrian plate tectonics. *Nature* 586 (7829), 395–401. <https://doi.org/10.1038/s41586-020-2806-7>.
- Ramnarine, R., Wagner-Riddle, C., Dunfield, K.E., Voroney, R.P., 2012. Contributions of carbonates to soil CO<sub>2</sub> emissions. *Can. J. Soil Sci.* 92, 599–607. <https://doi.org/10.4141/cjss2011-025>.
- Roeloffs, E., 1999. Earth science: radon and rock deformation. *Nature* 399 (6732), 104–105. <https://doi.org/10.1038/20072>.
- Royden, L.H., Burchfiel, B.C., King, R.W., Wang, E., Chen, Z., Shen, F., Liu, Y., 1997. Surface deformation and lower crustal flow in eastern Tibet. *Science* 276 (5313), 788–790. <https://doi.org/10.1126/Science.276.5313.788>.
- Shen, J.F., Santosh, M., Li, S.R., Zhang, H.F., Yin, N., Dong, G.C., Wang, Y.J., Ma, G.G., Yu, H.J., 2013. The Beiminghe skarn iron deposit, eastern China: geochronology,

- isotope geochemistry and implications for the destruction of the North China Craton. *Lithos* 156–159, 218–229. <https://doi.org/10.1016/j.Lithos.2012.11.003>.
- Skelton, A., Andr en, M., Kristmannsd ttir, H., Stockmann, G., M rth, C.M., Sveinbj rnisd ttir,  ., J nsson, S., Sturkell, E., Gu r nard ttir, H.R., Hjartarson, H., Siegmund, H., Kockum, I., 2014. Changes in groundwater chemistry before two consecutive earthquakes in Iceland. *Nat. Geosci.* 7 (10), 752–756. <https://doi.org/10.1038/ngeo2250>.
- Sun, Q., Zhao, C., L i, H., 2016a. Radon emission evolution and rock failure. *Acta Geod. Geophys.* 51 (3), 583–595. <https://doi.org/10.1007/s40328-015-0147-z>.
- Sun, X., Wang, G., Shao, Z., Si, X., 2016b. Geochemical characteristics of emergent gas and groundwater in Haiyuan fault zone. *Earth Sci. Front.* 23 (3), 140–150. <https://doi.org/10.13745/j.esf.2016.03.018> (in Chinese with an English abstract).
- Tamburello, G., Pondrelli, S., Chiodini, G., Rouwet, D., 2018. Global-scale control of extensional tectonics on CO<sub>2</sub> earth degassing. *Nat. Commun.* 9, 4608. <https://doi.org/10.1038/s41467-018-07087-z>.
- Tao, M., 2005. Characteristics of mantle degassing and deep-seated geological structures in different typical fault zones of China. *Sci. China Ser. D-Earth Sci.* 48 (7), 1074–1088.
- Wang, W.H., 2008. The Study of the Relationship between the Characteristics of the Deep Fluid and the Regional Seismic Activity in the Northern Margin Fault Zone of the Qinling. Lanzhou Institute of Seismology, China Earthquake Administration, Lanzhou. <https://doi.org/10.1016/j.epsl.2008.12.038> (in Chinese with an English abstract).
- Wang, M., Shen, Z.K., 2019. Present-day crustal deformation of continental China derived from GPS and its tectonic implications. *J. Geophys. Res.-Solid Earth* 125 (2). <https://doi.org/10.1029/2019JB018774>.
- Wang, F., Zhang, B., 1991. The Relation between the contents of rare-gases and trace-elements in hot springs and tectonic actives in the eastern GanSu province. *Northwest. Seismol. J.* 13 (4), 14–21 (in Chinese with an English abstract).
- Wang, Jun, Liu, Q., Chen, J., Cheng, L.S., Guo, B., Li, Y., 2009. Three-dimensional S-wave velocity structure of the crust and upper mantle beneath the Capital Circle Region from receiver function inversion. *Chin. J. Geophys.* 52 (10), 2472–2482. <https://doi.org/10.3969/j.issn.0001-5733.2009.10.006> (in Chinese with an English abstract).
- Weiss, R.F., 1971. Solubility of helium and neon in water and seawater. *J. Chem. Eng. Data* 16 (2), 235–241. <https://doi.org/10.1021/je60049a019>.
- Wu, F.Y., Lin, J.Q., Wilde, S.A., Yang, J.H., 2005. Nature and significance of the Early Cretaceous giant igneous event in eastern China. *Earth Planet. Sci. Lett.* 233 (1–2), 103–119. <https://doi.org/10.1016/j.epsl.2005.02.019>.
- Wu, P., Ding, Z., Tan, H., Yang, Q., Wang, X., 2021. Inversion MT data for the electrical structure beneath the Zhangbo seismic belt based on constraint of the V<sub>P</sub>/V<sub>S</sub> model. *Chin. J. Geophys.* 64 (8), 2716–2732. <https://doi.org/10.6038/cjg202100292> (in Chinese with an English abstract).
- Xu, S., Zheng, G., Wang, X., Wang, H., Nakai, S., Wakita, H., 2014. Helium and carbon isotope variations in Liaodong Peninsula, NE China. *J. Asian Earth Sci.* 90, 149–156. <https://doi.org/10.1016/j.jseaeas.2014.04.019>.
- Yang, Y., Li, Y., Guan, Z.J., Chen, Z., Zhang, L., Lv, C.J., Sun, F.X., 2018. Correlations between the radon concentrations in soil gas and the activity of the Anninghe and the Zemuhe faults in Sichuan, southwestern of China. *Appl. Geochem.* 89, 23–33. <https://doi.org/10.1016/j.apgeochem.2017.11.006>.
- Yuice, G., Italiano, F., D'Alessandro, W., Yalcin, T.H., Yasin, D.U., Gulbay, A.H., Ozyurt, N.N., Rojay, B., Karabacak, V., Bellomo, S., Brusca, L., Yang, T.F., Fu, C.C., Lai, C.W., Ozacar, A., Wallia, V., 2014. Origin and interactions of fluids circulating over the Amik Basin (Hatay-Turkey) and relationships with the hydrologic, geologic and tectonic settings. *Chem. Geol.* 388, 23–39. <https://doi.org/10.1016/j.chemgeo.2014.09.006>.
- Yuice, G., Fu, C., D'Alessandro, W., Gulbay, A., Lai, C., Bellomo, S., Yang, T., Italiano, F., Wallia, V., 2017. Geochemical characteristics of soil radon and carbon dioxide within the Dead Sea fault and Karasu fault in the Amik basin (Hatay), Turkey. *Chem. Geol.* 469, 129–146. <https://doi.org/10.1016/j.chemgeo.2017.01.003>.
- Zeng, G., He, Z.Y., Li, Z., Xu, X.S., Chen, L.H., 2016. Geodynamics of paleo-Pacific plate subduction constrained by the source lithologies of Late Mesozoic basalts in southeastern China. *Geophys. Res. Lett.* 43 (19), 10189–10197. <https://doi.org/10.1002/2016GL070346>.
- Zhai, M., 2019. Tectonic evolution of the North China Craton. *J. Geom.* 25 (5), 722–745. <https://doi.org/10.12090/j.issn.1006-6616.2019.25.05.063> (in Chinese with an English abstract).
- Zhai, M., Liu, W., 2003. Paleoproterozoic tectonic history of the North China craton: a review. *Precambrian Res.* 122 (1–4), 183–199. [https://doi.org/10.1016/S0301-9268\(02\)00211-5](https://doi.org/10.1016/S0301-9268(02)00211-5).
- Zhai, M., Santosh, M., 2013. Metallogeny of the North China Craton: link with secular changes in the evolving Earth. *Gondwana Res.* 24 (1), 275–297. <https://doi.org/10.1016/j.gr.2013.02.007>.
- Zhan, Y., Yang, H., Zhao, G., Zhao, Q., Sun, X., 2017. Deep electrical structure of crust beneath the Madongshan step area at the Haiyan fault in the northeastern margin of the Tibetan plateau and tectonic implications. *Chin. J. Geophys.-Chin. Ed.* 60 (6), 2371–2384. <https://doi.org/10.6038/cjg2017062>.
- Zhang, L., Wang, C., Cao, K., Wang, Q., Tan, J., Gao, Y., 2016. High elevation of Jiaolai Basin during the Late Cretaceous: implication for the coastal mountains along the East Asian margin. *Earth Planet. Sci. Lett.* 456, 112–123. <https://doi.org/10.1016/j.epsl.2016.09.034>.
- Zhang, Y.G., Zheng, W.J., Wang, Y.J., Zhang, D.L., Tian, Y.T., Wang, M., Zhang, Z.Q., Zhang, P.Z., 2018. Contemporary deformation of the North China plain from global positioning system data. *Geophys. Res. Lett.* 45 (4), 1851–1859. <https://doi.org/10.1002/2017GL076599>.
- Zhang, M., Guo, Z., Xu, S., Barry, P.H., Sano, Y., Zhang, L., Halld rsson, S.A., Chen, A.T., Cheng, Z., Liu, C.Q., Li, S.L., Lang, Y.C., Zheng, G., Li, Z., Li, L., Li, Y., 2021. Linking deeply-sourced volatile emissions to plateau growth dynamics in southeastern Tibetan Plateau. *Nat. Commun.* 12, 4157. <https://doi.org/10.1038/s41467-021-24415-y>.
- Zhao, Y., Zhai, M., Chen, H., Zhang, S., 2017. Paleozoic-early Jurassic tectonic evolution of North China Craton and its adjacent orogenic belts. *Geol. China* 44 (1), 44–60. <https://doi.org/10.12029/gc20170104>.
- Zhao, P., Chen, J., Li, Y., Liu, Q., Chen, Y., Guo, B., Yin, X., 2021. Growth of the northeastern Tibetan Plateau driven by crustal channel flow: evidence from high-resolution ambient noise imaging. *Geophys. Res. Lett.* 48 (13). <https://doi.org/10.1029/2021GL093387> e2021GL093387.
- Zheng, T., Zhao, L., Zhu, R., 2009. New evidence from seismic imaging for subduction during assembly of the North China craton. *Geology* 37 (5), 395–398. <https://doi.org/10.1130/G25600A.1>.
- Zheng, T.Y., He, Y.M., Yang, J.H., Zhao, L., 2015. Seismological constraints on the crustal structures generated by continental rejuvenation in northeastern China. *Sci. Rep.* 5 (1), 1–8. <https://doi.org/10.1038/srep14995>.
- Zhou, X.C., Wang, C.Y., Chai, C.Z., Si, X.Y., Lei, Q.Y., Li, Y., Xie, C., Liu, S.C., 2011. The geochemical characteristics of soil gas in the southeastern part of Haiyuan fault. *Seismol. Geol.* 33 (1), 123–132. <https://doi.org/10.3969/j.issn.0253-4967.2011.01.012> (in Chinese with an English abstract).
- Zhu, R., Xu, Y., Zhu, G., Zhang, H., Xia, Q., Zheng, T., 2012. Destruction of the North China craton. *Sci. China-Earth Sci.* 55 (10), 1565–1587. <https://doi.org/10.1007/s11430-012-4516-y>.